IEEE Access
Multidisciplinary ⋮ Rapid Review ⋮ Open Access Journal

Received September 15, 2021, accepted September 27, 2021, date of publication October 11, 2021,
date of current version October 25, 2021.

Digital Object Identifier 10.1109/ACCESS.2021.3119287

Full Solar-Spectrum Power-Generation System Based on High Efficiency and Wide Spectral Splitter Film and Fresnel Lens

DONG WANG[1,2], HOUZHI CAI[2], AND OU YANG[1]

[1]School of Artificial Intelligence, Shenhen Polytechnic, Shenzhen 518055 China
[2]Key Laboratory of Optoelectronic Devices and Systems of Ministry of Education and Guangdong Province, College of Physics and Optoelectronic Engineering, Shenzhen University, 518060, China

Corresponding author: Ou Yang (yangou@szpt.edu.cn)

This work was supported in part by the Guangdong Rural Science and Technology Correspondent Foundation under Grant KTP20200221, in part by the National Natural Science Foundation of China (NSFC) under Grant 11775147, in part by the Guangdong Basic and Applied Basic Research Foundation under Grant 2019A1515011474 and Grant 2019A1515110130, and in part by the Science and Technology Program of Shenzhen under Grant JCYJ20180305125443569 and Grant JCYJ20190808115605501.

ABSTRACT Based on high efficiency and wide spectral splitter film and Fresnel lens, we have theoretically investigated a full solar-spectrum power-generation system. Designed nano-multilayers are fabricated on Fresnel lens. Then short wavelengths (400 nm $\sim$ 1100 nm) of solar-spectrum can be transmitted 95% to the solar cell, and long wavelengths (1100 nm $\sim$ 2500 nm) of solar-spectrum can be reflected 90% and focused to the thermoelectric cell. This system can combine the efficiency of solar cells and thermoelectric cells to generate electricity across the entire solar spectrum. In theory, the limit for total conversion efficiency is $\eta = 56.64\%$.

INDEX TERMS Fresnel lens, full solar-spectrum, solar cell, thermoelectric cell.

I. INTRODUCTION

Solar-energy conversion usually takes one of two forms: the quantum approach, which uses the large per-photon energy of solar radiation to excite electrons, as in photovoltaic cells, or the thermal approach, which uses concentrated sunlight as a thermal-energy source to indirectly produce electricity using a heat engine.

In a photovoltaic (PV) cell, solar photons with energies above the semiconductor's bandgap excite electrons into the conduction band, which diffuse to electrodes and generate current. In high-performance solar cells, charge separation and collection are very efficient. However, the quantum approach of PV cells places intrinsic limitations on single-junction conversion efficiency. Photon energy in excess of the bandgap is lost as heat, known as thermalization loss, and sub-bandgap photons are not absorbed at all, known as absorption loss. In silicon solar cells, thermalization and absorption losses account for approximately 50% of the incident solar energy [1]. In principle, these losses could be reclaimed by using this waste heat from the PV cell to power a secondary thermal cycle. Combinations of PV and thermal engines are predicted to have efficiencies greater than 60% [2], yet fail in practice because PV cells rapidly lose efficiency at elevated temperatures [3], whereas heat engines rapidly lose efficiency at low temperatures [4].

Thermionic energy converters (TECs) are less well-known heat engines, which directly convert heat into electricity. A simple thermionic converter consists of a hot cathode and cooler anode separated by a vacuum gap. In the TEC cathode, fractions of the electrons have sufficient thermal energy to overcome the material's work function and escape into vacuum, generating current between the two electrodes. The thermionic current density is dictated by the cathode work function and temperature according to the Richardson–Dushman equation: $J = A_C^* T_C^2 e^{-\phi_C/kT_C}$, where ϕ_C is the cathode work function, T_C the temperature and A_C^* the materials-specific Richardson constant [5]. Thermionic converters were first proposed and fabricated in the 1950s, with experimental conversion efficiencies eventually reaching 10–15% [5], [6]. Both NASA and the Soviet space programme funded the development of TECs for

The associate editor coordinating the review of this manuscript and approving it for publication was Xiaodong Liang.

This work is licensed under a Creative Commons Attribution 4.0 License. For more information, see https://creativecommons.org/licenses/by/4.0/

deep-space missions and other applications requiring high-power autonomous generators, but the technology was never commercialized. Thermionic conversion's main challenges relate to the very high temperatures and substantial current densities required for efficient operation [7], [8].

These years, there is an increasing need for hybrid technologies for solar power generation. Photon-enhanced thermionic emission (PETE) combines photovoltaic and thermionic effects into a single physical process to take advantage of both the high per-quanta energy of photons, and the available thermal energy due to thermalization and absorption losses [9], [10]. Furthermore, the concept of solar thermophotovoltaic (STPV) system is introduced [11], [12], in which an intermediate element is placed between the sunlight and the solar cell. The intermediate element includes a black absorber — a material that can absorb the entire solar spectrum — on the side that faces the Sun. When exposed to sunlight, the element heats up and generates thermal radiation that is emitted through the other side, which is directed towards the photovoltaic cell. The fundamental advantage of this design is that virtually all-solar energy could be converted into electricity. However, despite their conceptual simplicity, STPV devices have performed below expectations and efficiencies have struggled to reach 3.2%.

Solar spectral splitting is a strategy to optimize the extraction of exergy from sunlight through the separation of incident photons by energy levels (or wavelengths). This approach generally implements any combination of thermal, electrical, or chemical processes that can increase the efficiency of a device [13]–[16].

Concentrated solar photovoltaic and photo-thermal conversion strategies each have their unique benefits and disadvantages, and the limiting efficiencies of both strategies have been discussed extensively. In order to take advantage of both technologies simultaneously, hybrid converters have been of great interest. The design of a number of these converters have been reported [17]–[20].

In this article, we have theoretically investigated a full solar-spectrum power-generation system based on high efficiency and wide spectral splitter film and Fresnel lens, which can combine the efficiencies of solar cells and thermoelectric cells to generate electricity across the entire solar spectrum. The characteristic of our system is the high efficiency and wide spectral splitter film. For short wavelength from 400 nm to 1150 nm, the transmittance is above 95%. For long wavelength from 1150 nm to 2500 nm, the reflectance is above 90%.

II. PRINCIPLE

As shown in Fig. 1, it is the diagram of our full solar-spectrum power-generation system. The splitter film is evaporated on the Fresnel lens. Therefore, short wavelengths (400 nm $\sim$ 1100 nm) of solar-spectrum can be transmitted to the solar cell, and long wavelengths (1100 nm $\sim$ 2500 nm) of solar-spectrum can be reflected and focused to the thermoelectric cell.

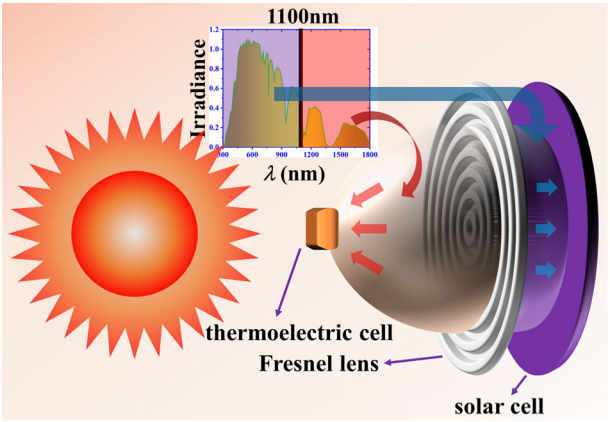

FIGURE 1. Diagram of full solar-spectrum power-generation system.

In the next sections, we shall further study the specific structure of the splitter film and Fresnel lens. A high efficiency and wide spectral splitter film is of great concern, and is difficult to design in technically and scientifically.

III. SPLITTER FILM

In this section, the theory of thin film optics (TFO) [21] is applied to design the splitter film, which can be used to design various functions of films. Based on FTO, we have studied quantum tunneling transparent conductive films [22] and anti-reflection nano multi-layers [23], [24].

These kind of nano multi-layers can be fabricated by low cost techniques, for example magnetron sputtering, electron beam evaporation, and thermal deposition process. Commercial software based on TFO is widely used to guide the industrial production of optical film, such as optical film design on lenses or glasses.

Full solar-spectrum is shown in Fig. 2. The dotted line is the solar spectrum at the top of the atmosphere, and the solid line is the solar spectrum at the sea level after being absorbed by H_2O vapor and CO_2.

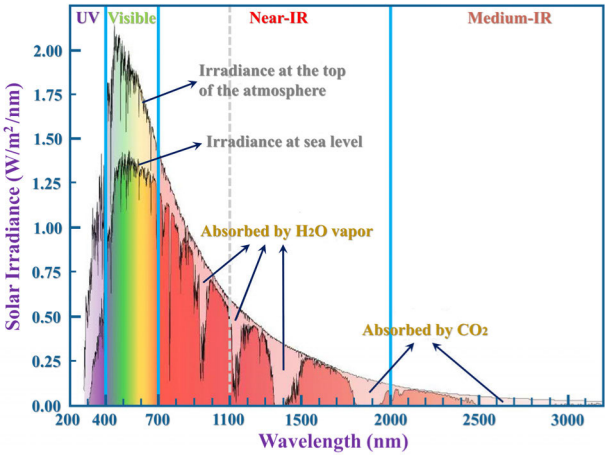

FIGURE 2. Diagram of full solar-spectrum system.

In our system as shown in Fig. 1, the splitter film should have the following function, that short wavelengths

(400 nm ∼ 1100 nm) of solar-spectrum are transmitted, and long wavelengths (1100 nm ∼ 2500 nm) of solar-spectrum are reflected.

In TFO design, low and high index materials are necessary to achieve the desired optical target. The materials should have low chromatic dispersity and no absorption. In this study, the low index material is MgF_2, and the high index material is Ta_2O_5. It's worth noting that the other low index material (such as SiO_2) and the other high index material (such as TiO_2) can also be used to design the splitter film. Once the material is selected, the thickness of every layer will determine the optimized result. Encouragingly, these thicknesses can be obtained by optical target optimization simulation of Essential Macleod or other commercial software. In this work, the film design and following results are obtained by Essential Macleod. Firstly, in Edit Generate window of Targets button, optimization goals can be set, i.e. transmittance and reflectance at different wavelength with different weight coefficients. Secondly, in Optimac Parameters window, Merit Function Power and Maximum Number of Layers can be set. Thirdly, press Refine button, and then Essential Macleod can optimize the layer number and thickness to meet the pre-set targets. Here, the transmittance target from 400 nm to 1150 nm is set to be 99% with weight 2, and the transmittance target from 1150 nm to 2500 nm is set to be 1% with weight 1. Finally, the number of layers and every layer thickness in Table 1 are automatic optimization by Essential Macleod for three months.

Optical target optimization simulation requires the knowledge of optical parameters of the materials. The refractive index N and extinction coeffificient K dependence on the wavelength (nm) for all the materials in this study can be obtained from the pioneer published works [24]–[27], as shown in Fig. 3. However, every different fabrication method with different condition will inflfluence the optical parameters of material, and then inflfluence the final designs. If researchers want to compare the experimental data with the theoretical results, they must obtain the optical property of every layer material in their experiment condition by ellipsometer.

Firstly, we should introduce the mathematical basics of energy transfer through the medium based on TFO. For the general case of assembly of q layers, the expression is

$$\begin{aligned}\begin{bmatrix} E_{i-s}^{(p,s)} \\ H_{i-s}^{(p,s)} \end{bmatrix} &= \left\{ \prod_{j=1}^{q} \begin{bmatrix} \cos\left(n_j k_0 d_j\right) & \pm i z_j \sin\left(n_j k_0 d_j\right) \\ \pm \frac{i}{z_j} \sin\left(n_j k_0 d_j\right) & \cos\left(n_j k_0 d_j\right) \end{bmatrix} \right\} \\ &\quad \times \begin{bmatrix} E_{o-s}^{(p,s)} \\ H_{o-s}^{(p,s)} \end{bmatrix} \\ &= \begin{bmatrix} T_{11} & \pm T_{12} \\ \pm T_{21} & T_{22} \end{bmatrix} \begin{bmatrix} E_{o-s}^{(p,s)} \\ H_{o-s}^{(p,s)} \end{bmatrix}, \end{aligned} \tag{1}$$

where the subscripts *i-s* and *o-s* means the physical quantities at the input surface boundary and the output surface boundary, respectively. In addition, k_0 is the wave vector in vacuum, z_j is the impedance ($z_j = z_0\sqrt{\mu_{r(j)}/\varepsilon_{r(j)}}$, $\mu_{r(j)}$ and $\varepsilon_{r(j)}$ are the relative permeability and relative permittivity), z_0 is the impedance in vacuum ($z_0 = \sqrt{\mu_0/\varepsilon_0}$, μ_0 and ε_0 are the permeability and permittivity in vacuum), and n_j is the refractive index($n_j = \sqrt{\varepsilon_{r(j)}\mu_{r(j)}}$). However, if we define $\exp[-i(\omega t - \vec{k}\cdot\vec{r})]$ as a wave propagating along the displacement vector $\vec{r}$, the form of Eq. 1 is a little different, where the imaginary part of the refractive index is positive for absorbing media.

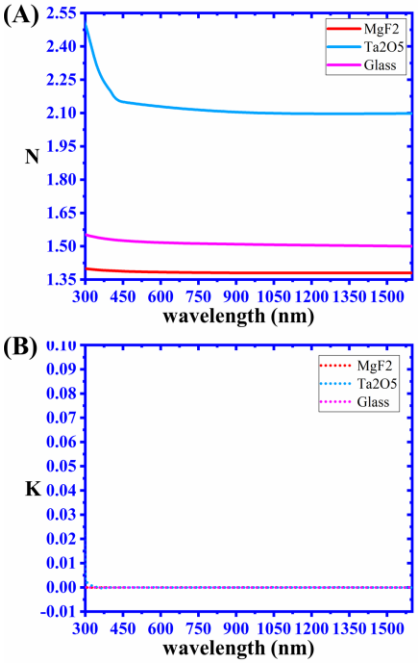

FIGURE 3. (A) Refractive index N dependence on the wavelength (nm) for the materials in this study; (B) extinction coefficient K dependence on the wavelength (nm) for the materials in this article.

From Eq. (1) amplitude reflection and transmission coefficients ρ and τ can be derived as

$$\rho^{(p,s)} = \frac{\mp z_{ou}T_{11} \mp T_{12} \pm z_{in}z_{ou}T_{21} \pm z_{in}T_{22}}{z_{ou}T_{11} + T_{12} + z_{in}z_{ou}T_{21} + z_{in}T_{22}}, \tag{2}$$

$$\tau^{(p,s)} = \frac{2z_{ou}}{z_{ou}T_{11} + T_{12} + z_{in}z_{ou}T_{21} + z_{in}T_{22}}, \tag{3}$$

where z_{in} and z_{ou} are the impedances of the input port medium and the output port medium, respectively. The net irradiance $\vec{I}$ is defined as $\vec{I} = \frac{1}{2}\mathrm{Re}\left(\vec{E}\times\vec{H}^*\right)$, and then the intense of net irradiance I can be expressed as $I = \frac{1}{2}\mathrm{Re}\left(EH^*\right) = \frac{1}{2}\mathrm{Re}\left(EE^*/z^*\right) = \frac{1}{2}EE^*\mathrm{Re}\left(1/z^*\right)$.The net irradiance reflection and transmission coefficients R_I and T_I can be expressed as

$$R_I = I_{re}/I_{in} = \rho^{(p,s)}\left(\rho^{(p,s)}\right)^*, \tag{4}$$

$$T_I = I_{ou}/I_{in} = \tau^{(p,s)}\left(\tau^{(p,s)}\right)^* \mathrm{Re}(1/z_{ou}^*)/\mathrm{Re}(1/z_{in}^*). \tag{5}$$

Here we have ignored the magnetic effect, and the relative permeability of all above materials is assumed to be 1.

However, there are many kinds of glass, for example white glass, electron-grade glass, and so on. Optical properties of these glasses are different. To simplify the problem, the substrate glasses in our following study are white glass. Generally, the relative permittivity of air is 1.

The detailed design of splitter film is in Table 1 of supplemental document by Essential Macleod, which has 189 layers of Ta_2O_5 and MgF_2, and the total thickness is 13.76 μm. The substrate is glass, and the incidence medium is air. Therefore, the material of Fresnel lens should be glass, which will be studied in detail in the next section.

The transmittance and reflectance properties of the splitter film are obtained, as shown in Fig. 4. The blue and red dotted lines are transmittance and reflectance, respectively. The wavelength varies from 350 nm to 2500 nm. For short wavelength from 400 nm to 1150 nm, the transmittance is above 95%. For long wavelength from 1150 nm to 2500 nm, the reflectance is above 90%. Therefore, this design of splitter film with high efficiency and wide spectral can meet our requirement for the full solar-spectrum power-generation system.

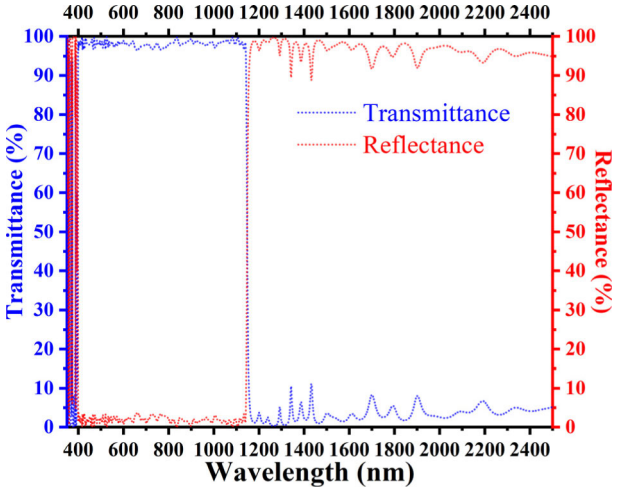

FIGURE 4. Transmittance (blue dotted line) and reflectance (red dotted line) dependence on the wavelength (nm) of the splitter film.

IV. FRESNEL LENS

The above splitter film has high efficiency and wide spectral. However, in order to reduce the occlusion of incident light and enhance the light thermal effect with a small size of the system structure, a flat and focusing device is also required. A large solar cell can be placed at the flat side, and the small thermoelectric cell can be placed at the focusing side. Therefore, Fresnel lens can meet our requirements. In this section, we should use geometrical optics to design the Fresnel lens. Fresnel lens is widely used to concentration light because of its flat and focusing characteristics [28]–[33].

In our full solar-spectrum power-generation system, the Fresnel lens should present reflectance and focusing peculiarities. Therefore, the Fresnel lens uses concave surface design, and the previously mentioned splitter film is fabricated on the concave side. In addition, for geometrical optics the reflectance angle is independent of wavelength. Hence, the position of the reflected focal point depends only on the geometry. However, for more sophisticated applications (for example super-resolution imaging), we need to consider diffractive optics, i.e. Fresnel diffraction formula, to study Fresnel lens.

As shown in Fig. 5, it is the diagram of design from concave lens to Fresnel lens. Sub-figure A is a concave lens (denoted as green pattern), which is a circle combined with the axis outside the paper 2D surface. Sub-figure B shows that the concave lens is divided into a lot rings, and each ring is removed from the part of the parallel plane (denoted as red pattern). Finally, the remaining parts constitute the Fresnel lens, as shown in sub-figure C. In geometrical optics, parallel plane cannot change the direction of light, nor can concentrate or diffuse light. Consequently, the remaining parts (in Fig. 5(C)) not only keep the reflectance and focusing peculiarities of concave lens (in Fig. 5(A)), but also has thinner structure, which can be easier to integrate smaller systems.

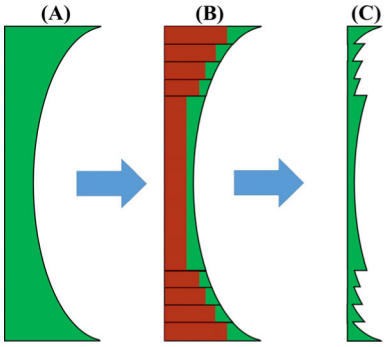

FIGURE 5. Diagram of design from concave lens to fresnel lens.

Here we use Geometrical Optics module of COMSOL Multiphysics (a commercial software based on finite element method) to study the Fresnel lens and obtain the following results. For more accuracy requirement, aspheric concave surface should be used to design the Fresnel lens. However, considering the cost and the accuracy of our experimental system, the spherical concave surface is adopted to design the Fresnel lens, as shown in Fig. 6(A).

The radius of the spherical concave surface is 150 mm. The diameter and thickness of our Fresnel lens are 190 mm and 12.5181 mm, respectively. There are eight order reflectors, which are the 1st reflector, the 2nd reflector, the 3rd reflector, etc., as denoted in Fig. 6(A). These reflectors are on a 5 mm thickness disk. The 1st reflector is a concave disk with diameter 50 mm and thickness 2.098 mm. The 2nd reflector is a concave doughnut with inner diameter 50 mm, outer diameter 70 mm, and thickness 2.0425 mm. The 3rd reflector is a concave doughnut with inner diameter 70 mm, outer diameter 90 mm, and thickness 2.7686 mm. The 4th reflector is a concave doughnut with inner diameter 90 mm, outer

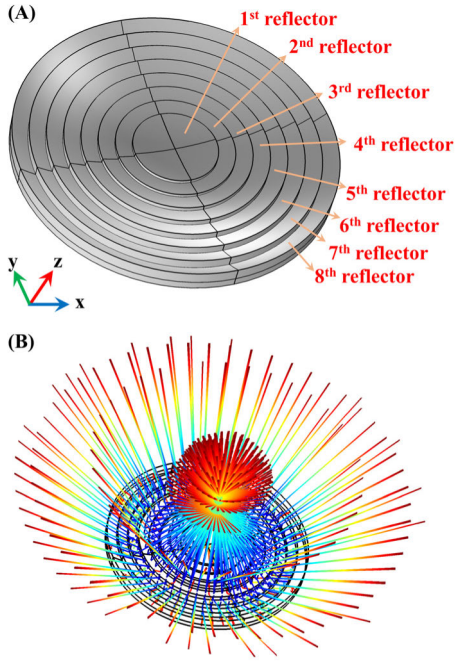

FIGURE 6. (A) Schematic diagram of fresnel lens with eight order reflectors; (B) 3D simulation results of incident ray reflection on fresnel lens.

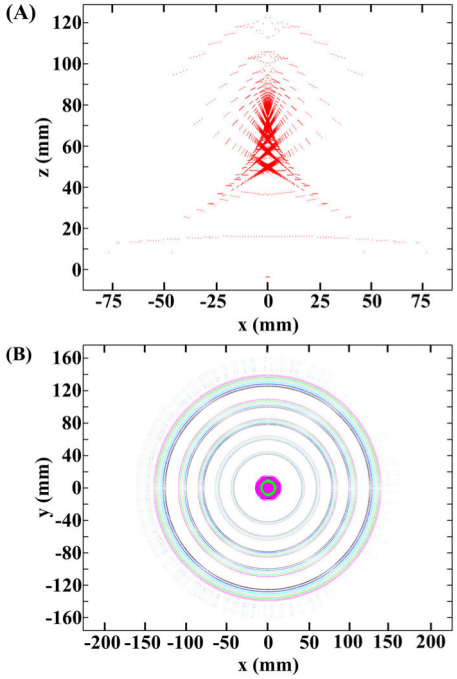

FIGURE 7. (A) poincare map of x-z plane with y = 0 mm; (B) Combined poincare map of x-y plane with z = 48 mm, 50 mm, 52 mm, 54 mm, 56 mm, and 58 mm.

diameter 110 mm, and thickness 3.5379 mm. The 5th reflector is a concave doughnut with inner diameter 110 mm, outer diameter 130 mm, and thickness 4.368 mm. The 6th reflector is a concave doughnut with inner diameter 130 mm, outer diameter 150 mm, and thickness 5.281 mm. The 7th reflector is a concave doughnut with inner diameter 150 mm, outer diameter 170 mm, and thickness 6.312 mm. The 8th reflector is a concave doughnut with inner diameter 170 mm, outer diameter 190 mm, and thickness 7.5181 mm.

As shown in Fig. 6(B), it is the 3D simulation results of incident ray reflection on Fresnel lens. It can be found that not all of the reflected rays will converge. A few rays at certain characteristic incidence points will be diffused by multiple reflections. In order to further investigate the convergence characteristics of rays, Poincare Maps is adopted. Generally, a cross section (called the Poincare cross section) is used to cut the track of continuous motion. Then, according to the situation of the track passing through the cross section, the shape of the motion can be simply judged, and the resulting image is called the Poincare Map. Fig. 7(A) is Poincare Map of x-z plane with y = 0 mm, Fig. 7(B) is combined Poincare Map of x-y plane with z = 48 mm (black points), 50 mm (blue points), 52 mm (cyan points), 54 mm (gray points), 56 mm (green points), and 58 mm (magenta points). What's more, Figs. 8(A)-(F) are separate Poincare Maps of x-y plane with z = 48 mm (A), 50 mm (B), 52 mm (C), 54 mm (D), 56 mm (E), and 58 mm (F), respectively.

These results show that the focus point is at z = 54 mm and the diameter of the focal spot is 20 mm. It means that thermoelectric cell should be placed at the 54 mm above the Fresnel lens, and physical size should be about 20 mm. Combined with the splitter film in section III, long wavelengths (1100 nm ∼ 2500 nm) of solar-spectrum can be reflected and focused to the thermoelectric cell, which is placed at a height of 54 mm; short wavelengths (400 nm ∼ 1100 nm) of solar-spectrum can be transmitted to the solar cell.

V. FULL SOLAR-SPECTRUM POWER-GENERATION SYSTEM

In this section we analyze the integration of the splitter film and Fresnel lens. As shown in Fig. 9, it's the diagram of the integration with the actual system. The main body of the system is an octahedral scaffold, which is convenient for large area parallel power generation. The upper and lower faces are a small circle and a large hexagon, respectively. The hexagonal frame with the side as 95mm holds a hexagonal Fresnel lens in place. Structural parameters of eight order reflectors for the hexagonal Fresnel lens are the same as that in section IV. Single crystalline silicon solar cell is nestled beneath the Fresnel lens, which is denoted by green color. The circle frame with the diameter as 20 mm is about 54 mm above the hexagonal frame, and holds a thermoelectric cell in place, which is denoted by red color. The splitter film in section III is evaporated on the upper surface of Fresnel lens.

The splitter separates incident photons based on their frequency. Low energy photons and high energy photons are directed towards the thermoelectric cell and solar cell, respectively.

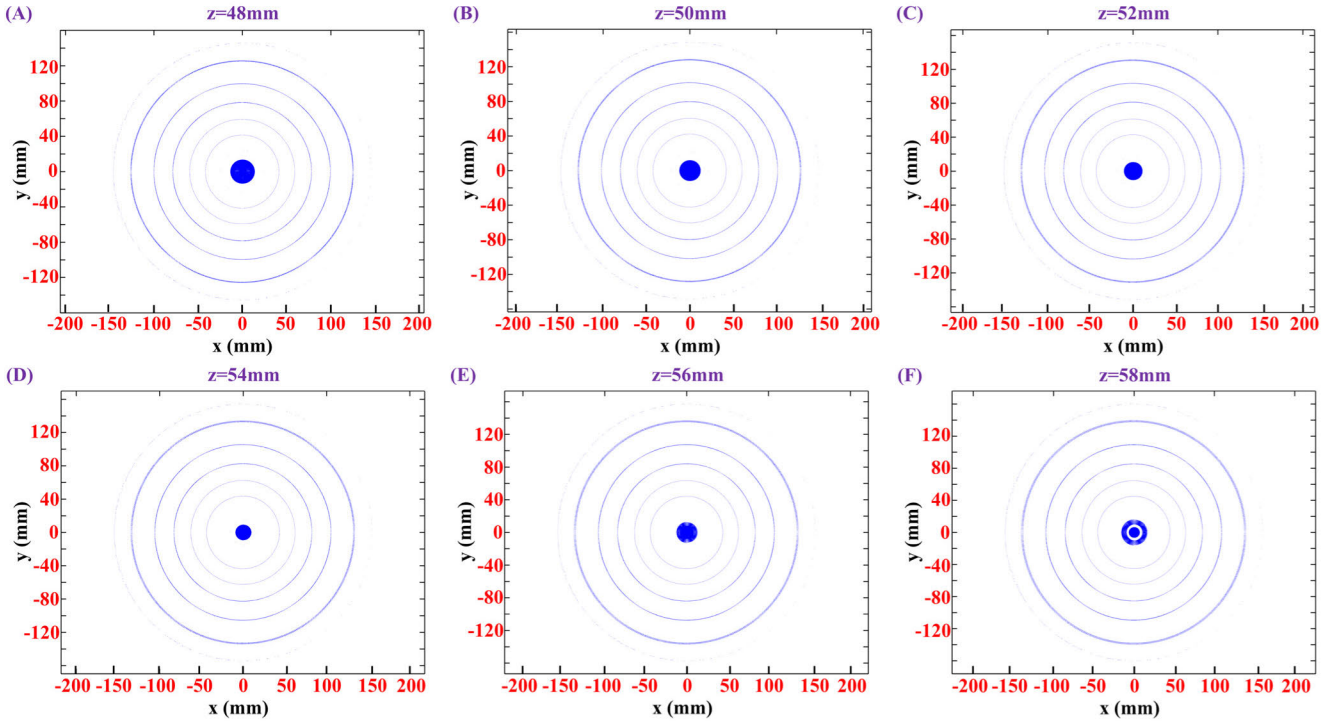

FIGURE 8. Separate poincare maps of x-y plane with (A) z = 48 mm (A), (B) z = 50 mm, (C) z = 52 mm, (D) z = 54 mm, (E) z = 56 mm, and (F) z = 58 mm.

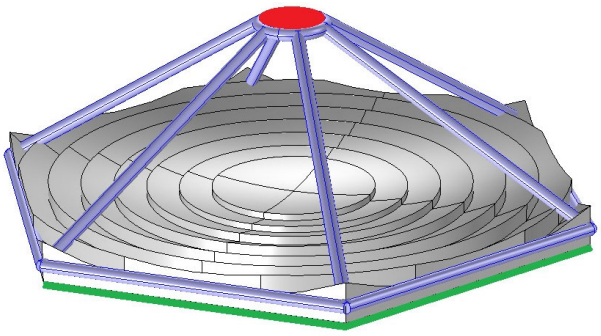

FIGURE 9. Diagram of the integration with the actual system, i.e. full solar-spectrum power-generation system.

The net heat gained can be determined by calculating the integral [14]

$$Q_{net} = \int_{\lambda_b}^{\lambda_c} \left[F_r(\lambda) G_s(\lambda) - 2 \int_0^{\theta_s} Q_{BB}(\lambda) \cos(\theta) \times \sin(\theta) \, d\theta \right] d\lambda, \quad (6)$$

where λ_b and λ_c are 1150 nm and 2500 nm, respectively. A blackbody source at $T_{sun} = 5777$ K (the thermodynamic temperature of the sun) generates a spectrum of electromagnetic radiation following the Planck distribution, denoted as $G_s(\lambda)$, as shown in Fig. 2. $F_r(\lambda)$ is the reflection splitter function of the splitter film, as shown in Fig. 4. θ is the zenith angle, and Q_{BB} is the blackbody spectrum characterized by T_H, which has the same functional form as G_s. This heat is then coupled to a thermal engine with a hot-side temperature equivalent to the absorber temperature and the cold-side temperature set at $T_{amb} = 300$ K. In the limiting case, thermodynamic work, W_{therm}, is extracted based on the Carnot efficiency between these two temperatures.

Meanwhile, photons that have wavelength within the spectral bandwidth (i.e., $\lambda_a \leq \lambda \leq \lambda_b$, $\lambda_a = 350nm$) are directed towards the solar cell. However, due to the applied voltage, radiative recombination is accounted for through the chemical potential, μ_c. Thus the generated photocurrent is given by

$$I_{pc} = IQE \cdot q \int_{\lambda_a}^{\lambda_b} \{F_t(\lambda) G_s(\lambda) - 2 \int_0^{\theta_s} \left(\frac{\hbar}{\lambda}\right)^2 \times \left[\exp\left(\frac{\hbar c/\lambda - \mu_c}{k_b T_c} \right) - 1 \right]^{-1} \times \cos(\theta) \sin(\theta) \, d\theta \} d\lambda, \quad (7)$$

where IQE is the internal quantum efficiency, q is the elementary charge, and kb is the Boltzmann constant. $F_t(\lambda)$ is the transmission splitter function of the splitter film, as shown in Fig. 4. The corresponding electrical power that the cell may extract from these carriers can be determined by

$$W_{elec} = \max\left(\mu_c \cdot I_{pc}(\mu_c)\right). \quad (8)$$

The sum of the output work from the thermal engine and the output work from the photovoltaic cell divided by the

TABLE 1. The detailed design of the splitter film.

Layer NO.	Materials	Thickness (nm)	Layer NO.	Materials	Thickness (nm)	Layer NO.	Materials	Thickness (nm)
0	Air		**64**	Ta_2O_5	42.89937	**128**	Ta_2O_5	21.32977
1	MgF_2	51.71955	**65**	MgF_2	53.20407	**129**	MgF_2	259.69906
2	Ta_2O_5	4.22155	**66**	Ta_2O_5	21.94274	**130**	Ta_2O_5	23.09756
3	MgF_2	274.01387	**67**	MgF_2	264.10853	**131**	MgF_2	32.22309
4	Ta_2O_5	2.5717	**68**	Ta_2O_5	13.45694	**132**	Ta_2O_5	187.41071
5	MgF_2	270.47401	**69**	MgF_2	72.33784	**133**	MgF_2	17.4695
6	Ta_2O_5	9.2387	**70**	Ta_2O_5	12.01048	**134**	Ta_2O_5	43.27685
7	MgF_2	44.71837	**71**	MgF_2	228.84759	**135**	MgF_2	51.59222
8	Ta_2O_5	23.48953	**72**	Ta_2O_5	16.7692	**136**	Ta_2O_5	18.1168
9	MgF_2	20.9308	**73**	MgF_2	31.82925	**137**	MgF_2	271.42701
10	Ta_2O_5	148.85342	**74**	Ta_2O_5	135.44975	**138**	Ta_2O_5	21.95846
11	MgF_2	30.66313	**75**	MgF_2	26.99464	**139**	MgF_2	33.57876
12	Ta_2O_5	32.89581	**76**	Ta_2O_5	14.78217	**140**	Ta_2O_5	165.13073
13	MgF_2	56.395	**77**	MgF_2	193.9065	**141**	MgF_2	24.73984
14	Ta_2O_5	31.68935	**78**	Ta_2O_5	20.69946	**142**	Ta_2O_5	27.91825
15	MgF_2	30.04779	**79**	MgF_2	23.75304	**143**	MgF_2	55.09443
16	Ta_2O_5	138.9335	**80**	Ta_2O_5	106.17488	**144**	Ta_2O_5	9.16619
17	MgF_2	26.70802	**81**	MgF_2	23.43532	**145**	MgF_2	286.12066
18	Ta_2O_5	20.84149	**82**	Ta_2O_5	21.58321	**146**	Ta_2O_5	9.64386
19	MgF_2	218.92962	**83**	MgF_2	196.80528	**147**	MgF_2	59.59409
20	Ta_2O_5	17.73781	**84**	Ta_2O_5	16.54104	**148**	Ta_2O_5	29.93136
21	MgF_2	33.8289	**85**	MgF_2	24.4517	**149**	MgF_2	24.8345
22	Ta_2O_5	26.9196	**86**	Ta_2O_5	130.78361	**150**	Ta_2O_5	171.90705
23	MgF_2	25.50192	**87**	MgF_2	27.71968	**151**	MgF_2	24.07403
24	Ta_2O_5	30.24752	**88**	Ta_2O_5	15.92809	**152**	Ta_2O_5	29.41023
25	MgF_2	45.31313	**89**	MgF_2	199.09464	**153**	MgF_2	56.78014
26	Ta_2O_5	11.59357	**90**	Ta_2O_5	17.42877	**154**	Ta_2O_5	10.82161
27	MgF_2	182.28908	**91**	MgF_2	28.41452	**155**	MgF_2	299.50055
28	Ta_2O_5	17.63684	**92**	Ta_2O_5	135.24715	**156**	Ta_2O_5	9.96083
29	MgF_2	30.87993	**93**	MgF_2	28.27022	**157**	MgF_2	65.76228
30	Ta_2O_5	129.03761	**94**	Ta_2O_5	19.24989	**158**	Ta_2O_5	30.36803
31	MgF_2	27.24608	**95**	MgF_2	229.55186	**159**	MgF_2	26.55888
32	Ta_2O_5	19.56179	**96**	Ta_2O_5	19.85777	**160**	Ta_2O_5	174.76038
33	MgF_2	229.78831	**97**	MgF_2	31.287	**161**	MgF_2	34.54368
34	Ta_2O_5	20.52038	**98**	Ta_2O_5	151.78617	**162**	Ta_2O_5	21.9435
35	MgF_2	53.77079	**99**	MgF_2	29.63127	**163**	MgF_2	269.13195
36	Ta_2O_5	32.10377	**100**	Ta_2O_5	19.70811	**164**	Ta_2O_5	20.93144
37	MgF_2	55.81128	**101**	MgF_2	231.10603	**165**	MgF_2	36.10282
38	Ta_2O_5	16.25578	**102**	Ta_2O_5	21.12613	**166**	Ta_2O_5	172.66406
39	MgF_2	65.55407	**103**	MgF_2	29.55938	**167**	MgF_2	31.74175
40	Ta_2O_5	2.3034	**104**	Ta_2O_5	156.08406	**168**	Ta_2O_5	28.93498
41	MgF_2	415.1504	**105**	MgF_2	26.56098	**169**	MgF_2	74.77937
42	Ta_2O_5	13.16443	**106**	Ta_2O_5	22.89099	**170**	Ta_2O_5	7.42963
43	MgF_2	45.86251	**107**	MgF_2	48.52169	**171**	MgF_2	166.51406
44	Ta_2O_5	38.49392	**108**	Ta_2O_5	5.98555	**172**	Ta_2O_5	2.07208

TABLE 2. *(Continued.)* **The detailed design of the splitter film.**

45	MgF_2	7.98036	**109**	MgF_2	300.51625	**173**	MgF_2	291.7251
46	Ta_2O_5	106.76736	**110**	Ta_2O_5	7.15447	**174**	Ta_2O_5	19.80802
47	MgF_2	35.55158	**111**	MgF_2	62.95008	**175**	MgF_2	37.74947
48	Ta_2O_5	19.77955	**112**	Ta_2O_5	26.22961	**176**	Ta_2O_5	167.57458
49	MgF_2	135.77407	**113**	MgF_2	29.7859	**177**	MgF_2	30.19941
50	Ta_2O_5	13.9637	**114**	Ta_2O_5	158.11123	**178**	Ta_2O_5	29.16785
51	MgF_2	46.8954	**115**	MgF_2	31.16896	**179**	MgF_2	73.92542
52	Ta_2O_5	145.70727	**116**	Ta_2O_5	18.21544	**180**	Ta_2O_5	7.91821
53	MgF_2	41.08905	**117**	MgF_2	221.82868	**181**	MgF_2	347.26749
54	Ta_2O_5	13.11727	**118**	Ta_2O_5	17.97645	**182**	Ta_2O_5	5.75514
55	MgF_2	165.79082	**119**	MgF_2	28.30916	**183**	MgF_2	70.05496
56	Ta_2O_5	19.8373	**120**	Ta_2O_5	150.43625	**184**	Ta_2O_5	26.46498
57	MgF_2	32.46388	**121**	MgF_2	32.18668	**185**	MgF_2	27.23552
58	Ta_2O_5	132.49225	**122**	Ta_2O_5	20.36132	**186**	Ta_2O_5	132.00538
59	MgF_2	13.3582	**123**	MgF_2	255.48007	**187**	MgF_2	10.77624
60	Ta_2O_5	39.48359	**124**	Ta_2O_5	21.38381	**188**	Ta_2O_5	23.45321
61	MgF_2	37.76742	**125**	MgF_2	32.84346	**189**	MgF_2	102.59333
62	Ta_2O_5	40.9021	**126**	Ta_2O_5	168.03541	**190**	Glass	
63	MgF_2	44.54066	**127**	MgF_2	32.24766			

input sun power to the system is defined as the efficiency

$$\eta_{total} = \frac{W_{therm} + W_{elec}}{\int_{\lambda_a}^{\lambda_c} G_s(\lambda)\, d\lambda} \times 100\%. \tag{9}$$

For our full solar-spectrum power-generation system, the bandgap of a typical Si solar cell is $E_G = 1.1$ eV, and the thermal collector temperature is $T_H = 666$ K (the dissociation temperature of one of the most common solar thermal heat transfer fluids, Therminol, VP-1 [34]). Therefore, the limit for total conversion efficiency is $\eta = 56.64\%$.

VI. CONCLUSION

We have theoretically investigated a full solar-spectrum power-generation system based on high efficiency and wide spectral splitter film and Fresnel lens, which provides a new way of thinking for the comprehensive utilization of all spectrum solar energy. Short wavelengths (400 nm $\sim$ 1100 nm) of solar-spectrum can be transmitted 95% to the solar cell, and long wavelengths (1100 nm $\sim$ 2500 nm) of solar-spectrum can be reflected 90% and focused to the thermoelectric cell. In theory, the limit for total conversion efficiency is $\eta = 56.64\%$. Our system is simple and cheap to manufacture and convenient for mass production. It makes sense not only in science but also in business. In the future, we will work on implementing our full solar-spectrum power-generation system, experimentally.

SUPPLEMENTAL DOCUMENT

See Table 1.

REFERENCES

[1] P. Würfel, *Physics of Solar Cells: From Basic Principles to Advanced Concepts*, 2nd ed. Hoboken, NJ, USA: Wiley, 2009.
[2] A. Luque and A. Martü, "Limiting efficiency of coupled thermal and photovoltaic converters," *Sol. Energy Mater. Sol. Cells*, vol. 58, no. 2, pp. 147–165, Jun. 1999.
[3] M. A. Green, "General temperature dependence of solar cell performance and implications for device modelling," *Prog. Photovolt., Res. Appl.*, vol. 11, no. 5, pp. 333–340, 2003.
[4] A. Kribus and G. Mittelman, "Potential of polygeneration with solar thermal and photovoltaic systems," *J. Sol. Energy Eng.*, vol. 130, no. 1, Feb. 2008, Art. no. 011001.
[5] G. N. Hatsopoulos, and E. P. Gyftopoulos, *Thermionic Energy Conversion*, vol. 1. Cambridge, MA, USA: MIT Press, 1973.
[6] G. N. Hatsopoulos and J. Kaye, "Measured thermal efficiencies of a diode iguration of a thermo electron engine," *J. Appl. Phys.*, vol. 29, pp. 1124–1125, 1958.
[7] *National Research Council Committee on Thermionic Research and Technology Thermionics Quo Vadis? An Assessment of the DTRA's Advanced Thermionics Research and Development Program*, National Academy, Thumbur, India, 2001.
[8] S. F. Adams, "Solar thermionic space power technology testing: A historical perspective," in *Proc. AIP Conf.*, Jan. 2006, vol. 813, no. 1, pp. 590–597.
[9] J. W. Schwede, I. Bargatin, D. C. Riley, B. E. Hardin, S. J. Rosenthal, Y. Sun, F. Schmitt, P. Pianetta, R. T. Howe, Z. X. Shen, and N. A. Melosh, "Photon-enhanced thermionic emission for solar concentrator systems," *Nature Mater.*, vol. 9, no. 9, pp. 762–767, 2010.
[10] D. Kraemer, B. Poudel, H. P. Feng, J. C. Caylor, B. Yu, X. Yan, Y. Ma, X. W. Wang, D. Z. Wang, A. Muto, K. McEnaney, M. Chiesa, Z. F. Ren, and G. Chen, "High-performance flat-panel solar thermoelectric generators with high thermal concentration," *Nature Mater.*, vol. 10, pp. 532–538, May 2011.

[11] R. M. Swanson, "A proposed thermophotovoltaic solar energy conversion system," *Proc. IEEE*, vol. 67, no. 3, pp. 446–447, Mar. 1979.
[12] A. Lenert, D. M. Bierman, Y. Nam, and W. R. Chan, "A nanophotonic solar thermophotovoltaic device," *Nature Nanotechnol.*, vol. 9, no. 2, pp. 126–130, Feb. 2014.
[13] A. G. Imenes and D. R. Mills, "Spectra beam splitting technology for increased conversion efficiency in solar concentrating systems: A review," *Sol. Energy Mater. Sol. Cells*, vol. 84, nos. 1–4, pp. 19–69, 2004.
[14] D. M. Bierman, A. Lenert, and E. N. Wang, "Spectral splitting optimization for high-efficiency solar photovoltaic and thermal power generation," *Appl. Phys. Lett.*, vol. 109, no. 24, Dec. 2016, Art. no. 243904.
[15] C. Kandilli and G. Külahli, "Performance analysis of a concentrated solar energy for lighting-power generation combined system based on spectral beam splitting," *Renew. Energy*, vol. 101, pp. 713–727, Feb. 2017.
[16] M. Tawfik, X. Tonnellier, and C. Sansom, "Light source selection for a solar simulator for thermal applications: A review," *Renew. Sustain. Energy Rev.*, vol. 90, pp. 802–813, Jul. 2018.
[17] T. P. Otanicar, S. Theisen, T. Norman, H. Tyagi, and R. A. Taylor, "Envisioning advanced solar electricity generation: Parametric studies of CPV/T systems with spectral filtering and high temperature PV," *Appl. Energy*, vol. 140, pp. 224–233, Feb. 2015.
[18] M. A. Hamdy, F. Luttmann, and D. Osborn, "Model of a spectrally selective decoupled photovoltaic/thermal concentrating system," *Appl. Energy*, vol. 30, no. 3, pp. 209–225, Jan. 1988.
[19] A. Mojiri, R. Taylor, E. Thomsen, and G. Rosengarten, "Spectral beam splitting for efficient conversion of solar energy—A review," *Renew. Sustain. Energy Rev.*, vol. 28, pp. 654–663, Dec. 2013.
[20] H. M. Branz, W. Regan, K. J. Gerst, J. B. Borak, and E. A. Santori, "Hybrid solar converters for maximum exergy and inexpensive dispatchable electricity," *Energy Environ. Sci.*, vol. 8, no. 11, pp. 3083–3091, 2015.
[21] H. A. Macleod, *Thin-Film Optical Filters*, 3rd ed. London, U.K.: Institute of Physics, 2001.
[22] D. Wang, J. Huang, Y. Lei, W. Fu, Y. Wang, P. Deng, H. Cai, and J. Liu, "Transparent conductive films based on quantum tunneling," *Opt. Exp.*, vol. 27, no. 10, pp. 14344–14352, 2019.
[23] D. Wang, Y. Wang, J. Huang, W. Fu, Y. Lei, P. Deng, H. Cai, and J. Liu, "Low-cost and flexible anti-reflection films constructed from nano multilayers of TiO_2 and SiO_2 for perovskite solar cells," *IEEE Access*, vol. 7, pp. 176394–176403, 2019.
[24] D. Wang, R. Zhou, Y. Wu, H. Cai, and Y. Zhang, "Improving external quantum efficiency by subwavelength nano multi-layered structures for optoelectronic devices," *IEEE Access*, vol. 8, pp. 189974–189981, 2020.
[25] N. Hong, R. A. Synowicki, and J. N. Hilfiker, "Mueller matrix characterization of flexible plastic substrates," *Appl. Surf. Sci.*, vol. 421, pp. 518–528, Nov. 2017.
[26] P. Prepelita, M. Filipescu, I. Stavarache, F. Garoi, and D. Craciun, "Transparent thin films of indium tin oxide: Morphology–optical investigations, inter dependence analyzes," *Appl. Surf. Sci.*, vol. 424, pp. 368–373, Dec. 2017.
[27] I. L. Elviyanti, H. Purwanto, and Kusumandari, "Optical simulation of surface textured TCO using FDTD method," *IOP Conf. Ser., Mater. Sci. Eng.*, vol. 107, Feb. 2016, Art. no. 012024.
[28] X.-T. Kong, A. A. Khan, P. R. Kidambi, S. Deng, A. K. Yetisen, B. Dlubak, P. Hiralal, Y. Montelongo, J. Bowen, S. Xavier, K. Jiang, G. A. J. Amaratunga, S. Hofmann, T. D. Wilkinson, Q. Dai, and H. Butt, "Graphene-based ultrathin flat lenses," *ACS Photon.*, vol. 2, no. 2, pp. 200–207, Feb. 2015.
[29] O. Yurduseven, D. L. Marks, J. N. Gollub, and D. R. Smith, "Design and analysis of a reconfigurable holographic metasurface aperture for dynamic focusing in the Fresnel zone," *IEEE Access*, vol. 5, pp. 15055–15065, 2017.
[30] J. M. Monkevich and G. P. Le Sage, "Design and fabrication of a custom-dielectric Fresnel multi-zone plate lens antenna using additive manufacturing techniques," *IEEE Access*, vol. 7, pp. 61452–61460, 2019.
[31] D. Podbiel, P. Kahl, B. Frank, T. J. Davis, H. Giessen, M. H.-V. Hoegen, and F. J. Meyer zu Heringdorf, "Spatiotemporal analysis of an efficient Fresnel grating coupler for focusing surface plasmon polaritons," *ACS Photon.*, vol. 6, no. 3, pp. 600–604, Mar. 2019.
[32] X. Sui, W. Li, Y. Zhang, and Y. Wu, "Theoretical and experimental evaluation of a thermoelectric generator using concentration and thermal energy storage," *IEEE Access*, vol. 8, pp. 87820–87828, 2020.
[33] A. F. Vaquero, M. R. Pino, M. Arrebola, S. A. Matos, J. R. Costa, and C. A. Fernandes, "Bessel beam generation using dielectric planar lenses at millimeter frequencies," *IEEE Access*, vol. 8, pp. 216185–216196, 2020.
[34] L. Moens and D. M. Blake, "Mechanism of hydrogen formation in solar parabolic trough receivers," *J. Sol. Energy Eng.*, vol. 132, no. 3, Aug. 2010, Art. no. 031006.

DONG WANG received the B.S. degree in optical information science and technology and the Ph.D. degree in optical engineering from the Huazhong University of Science and Technology, China, in 2009 and 2014, respectively. He is currently a Postdoctoral Researcher at the College of Physics and Optoelectronic Engineering, Shenzhen University, China. His research interests include optical films, quantum optics, transformation optics, and nano-structure optics.

HOUZHI CAI received the B.S. degree in optical information science and technology from the Huazhong University of Science and Technology, China, in 2004, and the M.S. and Ph.D. degrees in optical engineering from Shenzhen University, China, in 2007 and 2010, respectively. He is currently an Associate Professor at the College of Physics and Optoelectronic Engineering, Shenzhen University. His research interests include design and characterization of ultrafast sensors with sub-nanosecond temporal resolution and optical films.

OU YANG was born in Wuhan, Hubei, China, in 1979. He received the B.S. and M.S. degrees in computer science from the Wuhan University of Technology, Wuhan, China, in 2001 and 2004, respectively, and the Ph.D. degree in optical engineering from the Huazhong University of Science and Technology, Wuhan, in 2008. He is currently a Professor at the School of Artificial Intelligence, Shenhen Polytechnic, China. He is the author of three books, more than 20 articles, and more than 20 inventions. His research interests include machine vision, artificial intelligence, and optical measurement.